Phase Transition and Ionic Mobility in $LiHf_2(PO_4)_3$ with NASICON Structure

M. A. París,* A. Martínez-Juárez, J. E. Iglesias, J. M. Rojo, and J. Sanz

Instituto de Ciencia de Materiales de Madrid, Consejo Superior de Investigaciones Científicas (CSIC), Cantoblanco 28049, Madrid, Spain

Received January 16, 1997. Revised Manuscript Received March 25, 1997[⊗]

A reversible first-order phase transition has been found around 0 °C in the compound $LiHf_2(PO_4)_3$, which has been followed by DSC, XRD, NMR (^{31}P and ^{7}Li), and impedance techniques. In the low-temperature phase, a triclinic distortion of the NASICON framework has been detected for the first time in the $LiM_2(PO_4)_3$ family. In this phase location of lithium ions at low-symmetry sites (probably M_2 sites) has been deduced from ^{7}Li NMR data. Above 0 °C, the usual NASICON symmetry (rhombohedral $R\bar{3}c$) is recovered and an abrupt increase of the ionic mobility is observed: activation energy obtained from bulk dc conductivity decreases from 1.39 to 0.33 eV. From NMR data, a strong delocalization of lithium ions over M_1 and M_2 sites is detected when going from the triclinic to the rhombohedral phase.

I. Introduction

The finding of high sodium ion mobility in the NASICON ($Na_{1+x}Zr_2Si_xP_{3-x}O_{12}$) compounds[1,2] (acronym for Na SuperIonic CONductors) attracted much interest due to their potential application as solid electrolytes. Later on, this interest was extended to similar compounds in which Li atoms were substituted for Na and/or other tri- or tetravalent cations for Zr. In this family, ionic conductivity depends strongly on the amount of alkali element and the nature of the tri/tetravalent cation.[3−14]

In general, the NASICON framework is built up by $M_2(TO_4)_3$ units in which two MO_6 octahedra are linked by three TO_4 tetrahedra by oxygen sharing. Alkali ions can be placed in two different sites: one, in a distorted octahedral oxygen environment at the intersection of three conduction channels (M_1 site) and the other, at each bend of the conduction channels and surrounded by eight oxygens (M_2 site). The symmetry of the aristotype of these compounds is hexagonal $R\bar{3}c$,[15] although a lower-symmetry distortion has been found in some of them: $Na_{1+x}Zr_2Si_xP_{3-x}O_{12}$ with $x = 1.6$ and $x = 2.0$; $LiM^{IV}{}_2(PO_4)_3$ with M^{IV}= Zr and Sn. The first two compounds exhibit in the low-symmetry phase a monoclinic $C2/c$ structure,[16] but heating the samples above their corresponding phase transition temperature, the $R\bar{3}c$ symmetry is recovered. For the high-symmetry phase of these materials the best ionic conductivity value of the NASICON family (0.1 Ω^{-1} cm^{-1} at $T = 300$ °C) has been reported. In the second group of samples, ionic conductivity has been studied as a function of temperature, and structural changes involved in the phase transition analyzed.[14,17−19]

In this work, the structural phase transition of $LiHf_2(PO_4)_3$ has been analyzed using ^{31}P and ^{7}Li NMR (nuclear magnetic resonance), XRD (X-ray diffraction) and DSC (differential scanning calorimetry) techniques. The lithium mobility has been studied through the temperature dependence of the ionic conductivity and the ^{7}Li spin−spin (T_2) and spin−lattice (T_1) NMR relaxation times.

II. Experimental Section

The sample was prepared by calcination of a stoichiometric mixture of Li_2O, $(NH_4)_2H(PO_4)_3$ and HfO_2 at increasing temperatures in the range 850−1600 °C. A more detailed description of the sample preparation is reported elsewhere.[20]

X-ray powder diffraction patterns were recorded at room temperature and −40 °C by using a PW1050/25 Philips diffractometer. In these experiments, a 1° divergence slit, a diffracted beam curved graphite monochromator (Cu Kα = 1.540 598 1 Å), a 0.07° receiving slit, and a scintillation detector were used. Data were collected in the 2θ range 10−

* To whom all correspondence should be addressed.

[⊗] Abstract published in *Advance ACS Abstracts,* May 1, 1997.

(1) Goodenough, J. B.; Hong H. Y.; Kafalas, J. A. *Mater. Res. Bull.* **1976**, *11*, 203.
(2) Hong, H. Y. *Mater. Res. Bull.* **1976**, *11*, 173.
(3) Shannon, R. D.; Taylor, B. E.; English, A. D.; Berzins, T. *Electrochem. Acta* **1977**, *22*, 783.
(4) Taylor, B. E.; English, A. D.; Berzins, T. *Mater. Res. Bull.* **1977**, *12*, 171.
(5) Subramanian, M. A.; Subramanian, R.; Clearfield, A. *Solid State Ionics* **1986**, *18/19*, 562.
(6) Hamdoune, S.; Tran Qui, D.; Schouller, E. J. L. *Solid State Ionics* **1986**, *18/19*, 587.
(7) Li, S.; Cai, J.; Lin, Z. *Solid State Ionics* **1988**, *28/30*, 1265.
(8) Chowdari, B. V. R.; Radhakrishnan, K.; Thomas, K. A.; Subba Rao, G. V. *Mater. Res. Bull.* **1989**, *24*, 221.
(9) Aono, H.; Sugimoto, E.; Sadaoka, Y.; Imanaka, N.; Adachi, G. *J. Electrochem. Soc.* **1990**, *137*, 1023.
(10) Aono, H.; Sugimoto, E.; Sadaoka, Y.; Imanaka, N.; Adachi, G. *Solid State Ionics* **1991**, *47*, 257.
(11) Winand, J.; Rulmont, A.; Tarte, P. J. *Solid State Chem.* **1991**, *93*, 341.
(12) Aono, H.; Sugimoto, E.; Sadaoka, Y.; Imanaka, N.; Adachi, G. *J. Electrochem. Soc.* **1993,** *140*, 1827.
(13) Kuwano, J.; Sato, N.; Kato, M.; Takano, K. *Solid State Ionics* **1994**, *70/71*, 332.
(14) Martínez-Juárez, A.; Rojo, J. M.; Iglesias, J. E.; Sanz, J. *Chem. Mater.* **1995**, *7*, 1857.
(15) Hagman, L.; Kierkegaard, P. *Acta Chem. Scand.* **1968**, *22*, 1822.
(16) Didisheim, J.-J.; Prince, E. ; Wuensch, J. *Solid State Ionics* **1986**, *18/19*, 944.
(17) Petit, D.; Colomban, Ph.; Collin, G.; Boilot, J. P. *Mater. Res. Bull.* **1986**, *21*, 365.
(18) Sudreau, F.; Petit, D.; Boilot, J. P. *J. Solid State Chem.* **1989**, *83*, 78.
(19) Angenault, J.; Couturier, J. C.; Souron, J. P.; Siliqi, D.; Quarton, M. J. *Mater. Science Lett.* **1992**, *11*, 1705.
(20) Martínez-Juárez, A.; Iglesias, J. E.; Rojo, J. M. *Solid State Ionics* **1996**, *91*, 295.

S0897-4756(97)00041-0 CCC: $14.00

70° with a step size ranging between 0.02° and 0.04° and a counting time of 0.5 s/step. The low-temperature data were obtained with an Anton Paar HT camera, in which the sample was thinly spread over a platinum strip. The camera was modified so that dry cold nitrogen gas could be directly blown over the edge of the Pt strip. A room-temperature pattern was first taken and, then the temperature was lowered to −40 °C and a new pattern measured. The Pt lines, visible in both patterns, were used to calibrate the low-temperature pattern with respect to the room-temperature one.

A differential scanning calorimeter (Seiko 220CU) was used to determine the enthalpy associated with the structural transformation. The experiments were carried out under N_2 flow between −123 and 100 °C with heating and cooling rates of 5 °C/min.

Electrical conductivity measurements were carried out by the complex impedance method in a 1174 Solartron frequency response analyzer. Self-supporting pellets (ca. 6 mm diameter and 1 mm thickness) were prepared by compressing at 2000 kg/cm^2 the powder sample. Then, the pellets were sintered at 1050 °C in air. Gold electrodes were deposited on the two faces of the pellets by vacuum evaporation. The frequency range used was 10^{-1}−10^5 Hz. The measurements were carried out at different temperatures in heating and cooling runs with the pellet under nitrogen flow.

^{31}P and ^{7}Li NMR spectra, recorded in static and MAS conditions, were obtained at different temperatures between 22 and −43 °C by using a B-VT 1000/SU07 unit adapted to an MSL 400 Bruker spectrometer. The frequency used for ^{31}P and ^{7}Li spectra were 161.96 and 155.5 MHz, respectively. Spectra were taken after $\pi/2$ pulse irradiation. A time interval between successive scans in the range 2−30 s was chosen, depending on the spin−lattice relaxation times of the two nuclei at each temperature. The number of accumulations was in the range 10−200. The ^{7}Li and ^{31}P chemical shifts values are given relative to 1 M LiCl and 85% H_3PO_4 aqueous solutions, respectively. The fitting of NMR spectra was carried out with the Bruker WINFIT program,[21] which computes the intensities of the sidebands by the Herzfeld and Berger method.[22] With this program, the position, line width, and intensity of the components are determined with a standard nonlinear least-squares method. However, the anisotropies and asymmetry parameters, which characterize nuclear interactions, have to be determined by a trial and error procedure.

The temperature dependence of the ^{7}Li spin−lattice (T_1) and spin−spin (T_2) relaxation times of static sample was obtained with a SXP 4/100 Bruker spectrometer. The frequency used was 31.01 MHz . The experiments were carried out between −170 and 230 °C. T_1 values at each temperature were determined by using the classical $\pi-\tau-\pi/2$ sequence.[23] To that end, the recovery of experimental magnetization was fitted to the exponential function

$$M(\tau) = M_0[1 - 2\exp(-(\tau - t_0)/T_1)] \qquad (1)$$

where the spin−lattice relaxation time (T_1), the thermal equilibrium magnetization (M_0), and the time t_0 were considered free parameters in a least-squares fitting procedure. On the other hand, T_2 values were obtained from single-pulse experiments:[23] T_2^{-1} values were calculated as 0.6π times the full width at half-height (fwhh) for a Gaussian line and as π times fwhh for a Lorentzian line.

III. Results

III.1. DSC. The calorimetric curves, obtained by cooling the sample between 25 and −120 °C and then by heating the sample from −120 to 100 °C, are shown in Figure 1. In the cooling treatment (Figure 1a), a broad exothermic peak appears, whose onset and maximum temperature are −4 and −13 °C, respectively. An enthalpy of −4.48 kJ/mol is deduced. In the heating treatment (Figure 1b) a narrow endothermic peak with onset and maximum temperatures of 0 and 7.5 °C is observed. The enthalpy deduced from this peak is 4.54 kJ/mol. From these data a small hysteresis is detected (∼5 °C). To avoid any effect due to this hysteresis, all the experiments described hereafter were carried out during sample cooling treatments.

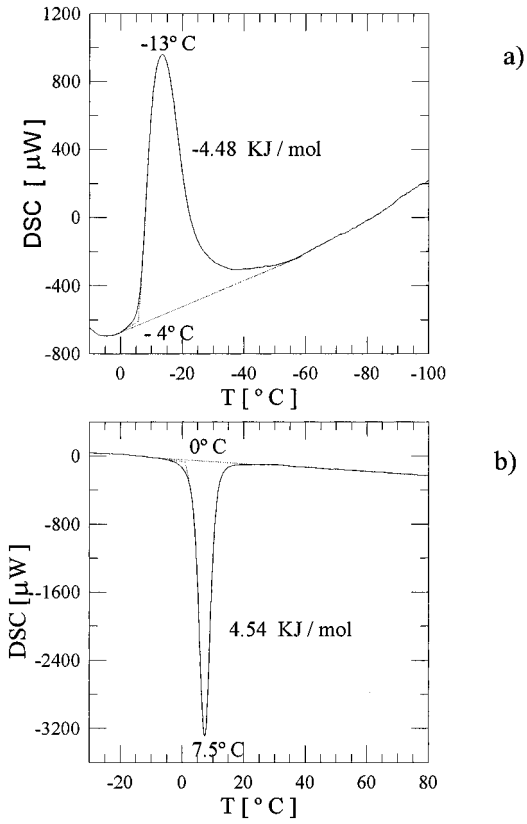

Figure 1. DSC curves corresponding to the (a) cooling and (b) heating runs of $LiHf_2(PO_4)_3$. The onset and maximum temperatures and the entalphy associated to each treatment are also indicated in the figure.

III.2. XRD. The X-ray diffraction patterns recorded at room temperature and −40 °C are shown in Figure 2, where only the lower 2θ region is shown to emphasize splittings. The pattern obtained at room temperature is similar to that reported by other authors,[3−5,8,24] who indexed it on the basis of a rhombohedral $R\bar{3}c$ lattice, by using hexagonal axes. The pattern obtained at −40 °C shows more peaks as a consequence of the splitting of some hexagonal reflections, indicating a change of symmetry. Thus, for instance, the$(024)_{hex}$ reflection produces three resolved peaks with similar intensities and the $(104)_{hex}$ and $(110)_{hex}$ lines are split into a total of five peaks.

III.3. NMR. ^{31}P ($I = {}^1/_2$) static and MAS NMR spectra, recorded at room temperature and −23 °C are displayed in Figure 3. In the static spectra a single component, broader in the spectrum obtained at lower temperature, is resolved. This component is strongly narrowed when the sample is spun in MAS experiments;

(21) Massiot, D. WINFIT programme, Bruker-Franzen Analytik GmbH, 1993.
(22) Herzfeld, J.; Berger, E. *J. Chem. Phys.* **1980**, *73*, 6021.
(23) Fukushima, E.; Roeder, S. B. W. *Experimental Pulse NMR (A Nuts and Bolts Approach)*; Addison-Wesley: Reading, MA, 1981.
(24) Sljukic, M.; Matkovic, B.; Prodic, B.; Scavnicar, S. *Croat. Chem. Acta* **1967**, *39*, 145.

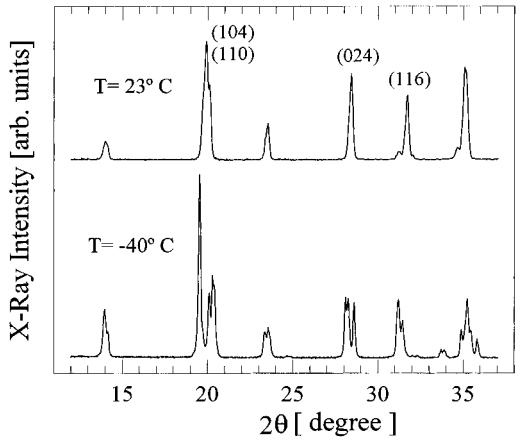

Figure 2. X-ray diffraction patterns of $LiHf_2(PO_4)_3$ recorded at the indicated temperatures. Only the low 2θ region (13−37°) is shown to emphasize splittings. Miller indices of hexagonal reflections mentioned in the text are also included.

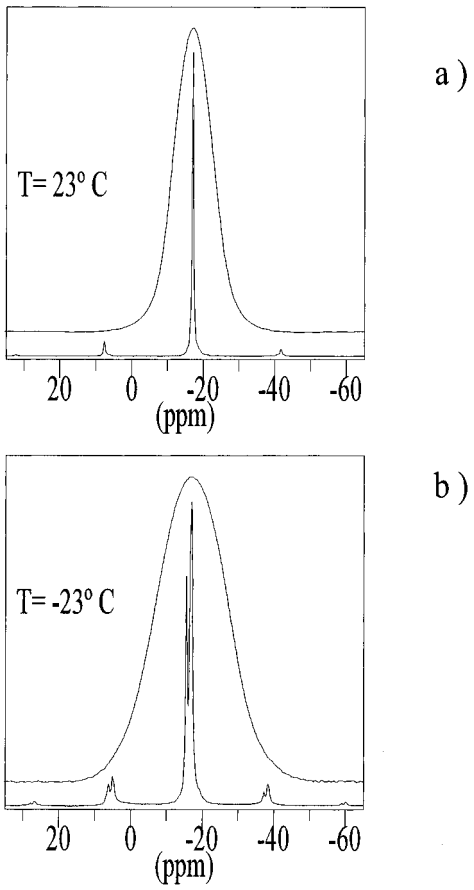

Figure 3. ^{31}P static and MAS NMR spectra recorded at (a) 23 °C and (b) −23 °C. MAS spectra were obtained at a spinning rate of $\nu_r \approx 4000$ Hz.

then one or several central components, with their corresponding spinning sidebands spaced at ∼25 ppm (spinning rate of the sample expressed in ppm) are resolved. At 23 °C (Figure 3a) a single line at −17.1 ppm is detected. However, the spectrum recorded at −23 °C (Figure 3b) is constituted by three components at −15.5, −16.5, and −17.0 ppm, which exhibit the same integrated intensities.

^7Li ($I = {}^3/_2$) static and MAS spectra, obtained at room temperature and −23 °C, are plotted in Figure 4. Static spectra are formed by a central line and a broad symmetric pattern. The line width of the central

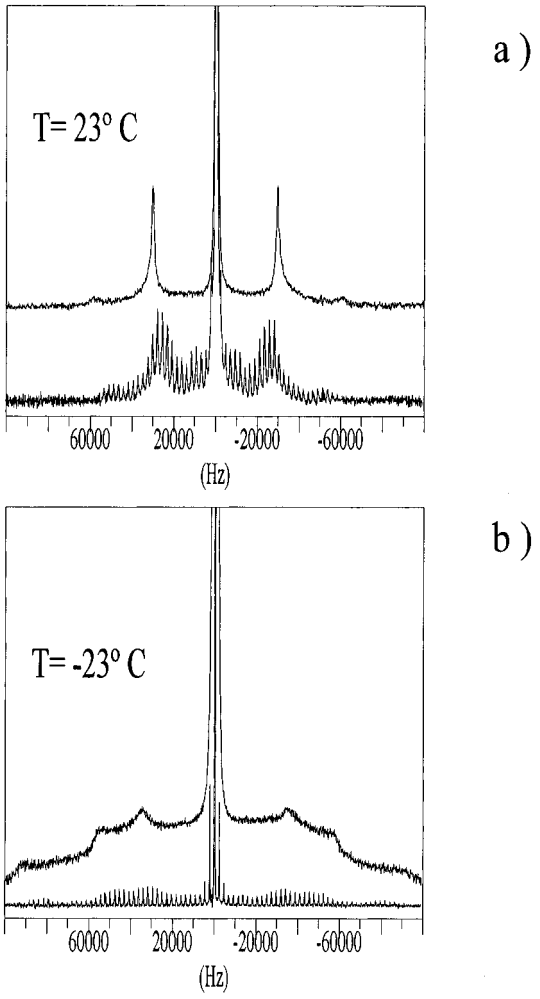

Figure 4. ^7Li static and MAS NMR spectra of $LiHf_2(PO_4)_3$ recorded at (a) 23 °C and (b) −23 °C. Spinning rate of MAS spectra is $\nu_r \approx 2000$ Hz.

transition ($-{}^1/_2 \rightarrow {}^1/_2$ transition) narrows and its line shape changes from Gaussian to Lorentzian when going from the spectrum obtained at −23 °C to the room-temperature one. Detection of the broad symmetric pattern ($^1/_2 \rightarrow {}^3/_2$, $-{}^3/_2 \rightarrow -{}^1/_2$ satellite transitions) is caused by the interaction of the quadrupole moment of nuclei with the electric field gradient at structural sites.[25] It can be seen that the quadrupole pattern of the low-temperature spectrum is different and covers a wider frequency range than that of the room-temperature spectrum (Figure 4a,b). On the other hand, the central and external transitions are modulated by the spinning sidebands in MAS experiments, allowing a better analysis of the quadrupole pattern. From both kind of spectra, determination of the quadrupole coupling constant, C_Q, and the asymmetry parameter, η, has been done. From the spectra recorded at room temperature, values of $\eta = 0.0$ and $C_Q = 116$ kHz were deduced; while from the spectra recorded at −23 °C values of $\eta = 0.3$ and $C_Q = 180$ kHz were obtained.

In Figure 5 the evolution of the central component of ^{31}P and ^7Li MAS NMR spectra between 5 and −23 °C is displayed. In ^{31}P MAS spectra (Figure 5a), it is observed that the single line present at room temperature decreases and that three new lines of equal

(25) Abragam, A. *The Principles of Nuclear Magnetism*; Oxford University Press: Oxford, 1961.

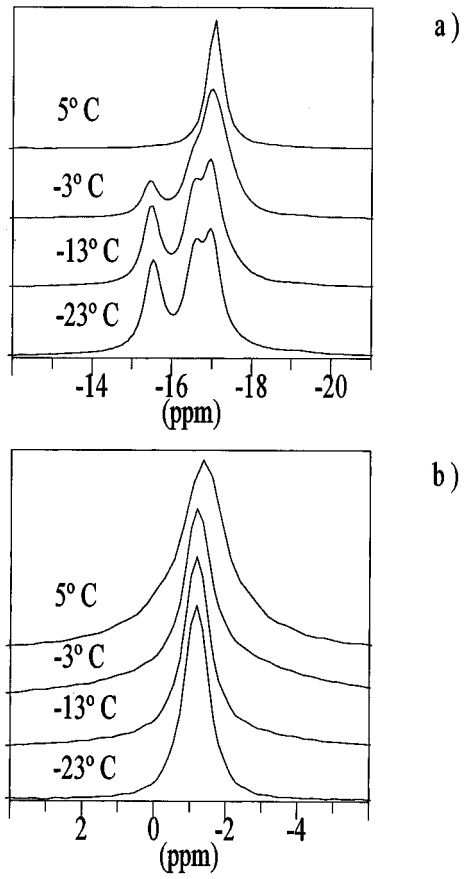

Figure 5. (a) ^{31}P and (b) ^{7}Li central component of MAS NMR spectra recorded at the indicated temperatures.

relative intensity become resolved during sample cooling. One of the new lines (−17.0 ppm) has practically the same position as the starting one (−17.1 ppm). On the other hand, ^{7}Li MAS spectra (Figure 5b) show a single central line for all temperatures, which becomes narrower and moves slightly to less negative chemical shift when the temperature is decreased.

The temperature dependence of C_Q is displayed in Figure 6a. C_Q shows a clear discontinuity about 0 °C and remains almost constant above and below this temperature. A similar trend, not displayed in the figure, is observed for η: it takes on values of 0.3 and 0.0 below and above the mentioned temperature. Finally, the temperature dependence of the spin−spin (T_2) and spin−lattice (T_1) relaxation times of the central transition of static ^{7}Li NMR spectra exhibits also a discontinuity near 0 °C (Figure 6b,c). T_2^{-1} and T_1^{-1} are constant below this temperature, change drastically at 0 °C and decrease very slightly above this temperature.

III.4. Impedance Spectroscopy. The impedance plots (imaginary vs real part) recorded at different temperatures are shown in Figure 7. At 27 and 60 °C two arcs and one spike are observed. The spike is due to the blocking effect of lithium ions at the electrodes. According to a previous study,[20] the arcs have been ascribed to movement of lithium ions inside the grains (high-frequency arc) and through grain boundaries (low-frequency arc). At lower temperatures (−7 and −19 °C) only the high-frequency arc is observed over the analyzed frequency range. The resistance associated with the high-frequency arc is deduced from intersection of the arc with the real axis. Then, the conductivity values are obtained as usual.

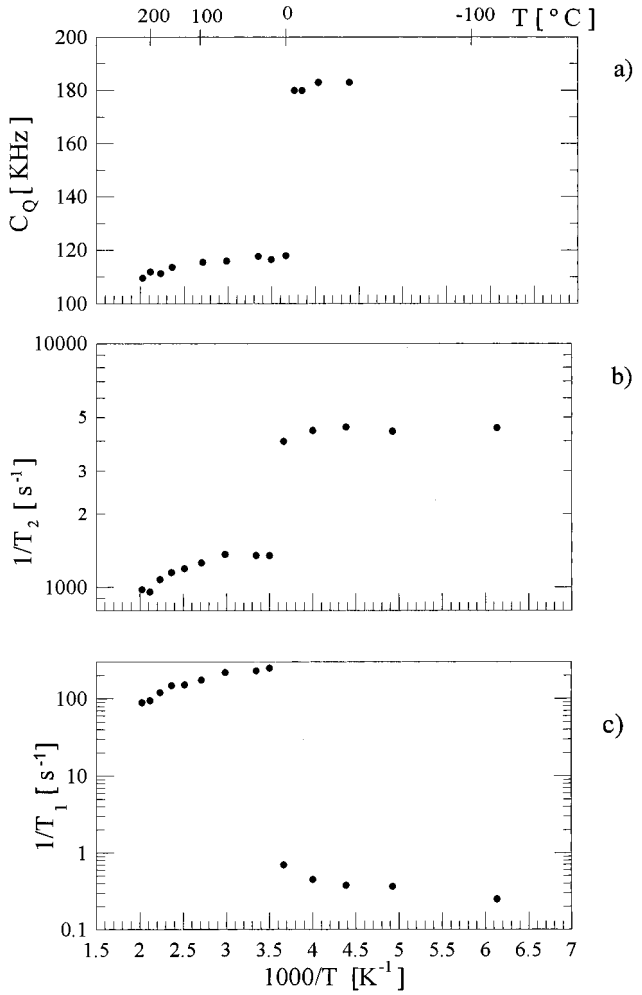

Figure 6. Temperature dependence of the (a) quadrupole coupling constant (C_Q), the (b) spin−spin (T_2^{-1}), and (c) spin−lattice (T_1^{-1}) relaxation rates.

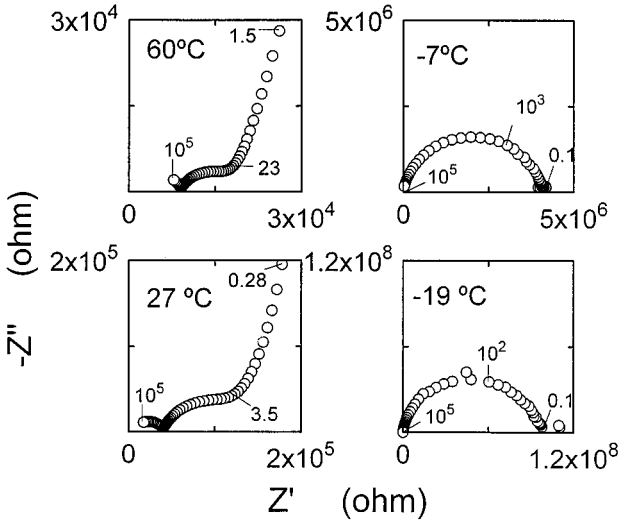

Figure 7. Impedance plots (imaginary $-Z''$ vs real Z' part) recorded at the indicated temperatures.

The variation of the bulk conductivity (log σ_b), associated to the high-frequency arc, versus inverse temperature (1000/T) is shown in Figure 8. Two linear dependencies are observed: one above 0 °C and the other below this temperature. From the fitting of the experimental data to the Arrhenius equation, $\sigma = \sigma_0 \exp(-E/kT)$, the activation energy (E) and preexponen-

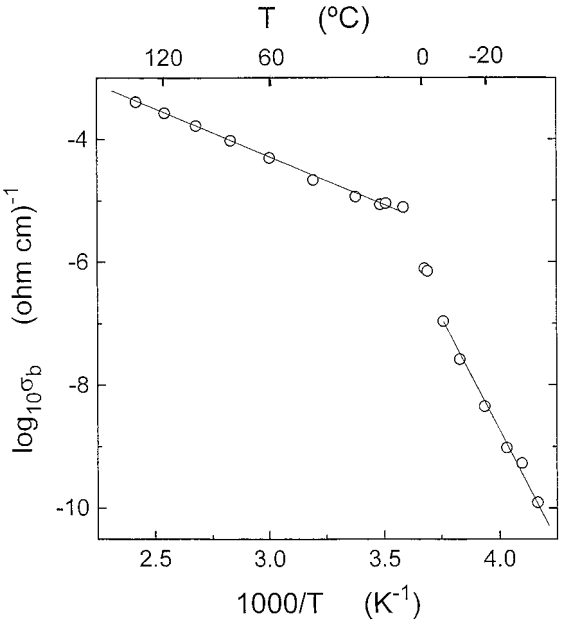

Figure 8. Variation of the bulk dc conductivity ($\log_{10}\sigma$) versus inverse temperature (1000/T).

tial factor (σ_0) corresponding to the two regions have been determined. The values for E and σ_0 are 0.33 eV and 4 Ω^{-1} cm^{-1} for temperatures above 0 °C and 1.39 eV and 1.7 × 10^{19} Ω^{-1} cm^{-1} below 0 °C.

IV. Discussion

IV.1. Phase Transition. The X-ray diffraction pattern recorded at room temperature has been indexed[20] on the basis of a rhombohedral $R\bar{3}c$ lattice of hexagonal parameters $a_H = 8.8295$ and $c_H = 22.019$ Å. These values are very close to those reported by other authors.[3−5,8,24] The rhombohedral $R\bar{3}c$ symmetry is supported by NMR data. Thus, the room-temperature ^{31}P MAS spectrum shows a single line at −17.1 ppm, indicating only one crystallographic site for phosphorus. When the sample is cooled below 0 °C, a splitting of the rhombohedral X-ray peaks is observed. The $(024)_{hex}$ reflection produces three resolved peaks with similar intensities, and the incompletely resolved $(104)_{hex}$ and $(110)_{hex}$ reflections give at least five new peaks. A monoclinic distortion of the rhombohedral lattice of the type documented in the literature should lead to no more than two peaks for the splitting of the $(024)_{hex}$: the $(400)_{mon}$ and $(\bar{2}22)_{mon}$, and no more than four peaks for the splitting of the $(\underline{1}04)_{hex}$ and $(110)_{hex}$ as follows: $(\underline{1}04)_{hex} \rightarrow (111)_{mon} + (\bar{2}02)_{mon}$, $(110)_{hex} \rightarrow (020)_{mon} + (\bar{3}11)_{mon}$. Therefore, the experimental data point to a structure of lower symmetry. On these bases, 29 reflections were indexed with a nonconventional triclinic C-cell of parameters $a = 15.26(1)$, $b = 8.689(3)$, $c = 9.067(9)$ Å, $\alpha = 89.44(6)°$, $\beta = 123.78(7)°$, $\gamma = 90.61(6)°$, V = 999.5 Å^3. The triclinic C-centered cell was chosen to preserve the relationship to the usual monoclinic distortion of rhombohedral NASICON. The lattice can also be characterized by its reduced Niggli cell, whose parameters were calculated by the algorithm of Křivý & Gruber,[26] to obtain the following values: $a_N = 8.689$, $b_N = 8.740$, $c_N = 9.067$ Å, $\alpha_N = 118.72°$, $\beta_N = 90.56°$, $\gamma_N = 119.20°$, $V_N = 499.6$ Å. The triclinic symmetry is consistent with NMR data: the ^{31}P MAS spectrum obtained at −23 °C shows three lines of the same intensity indicating the existence of three crystallographically nonequivalent sites for phosphorus. The same symmetry, with very similar lattice parameters, has also been deduced very recently from neutron diffraction of a compound with similar composition by Losilla et al.[27]

Table 1. Cell Parameters of the Triclinic and Rhombohedral Phases[a]

parameters	triclinic	rhombohedral	rel variation (%)
a (Å)	15.26(1)	15.294(9)	0.2
b (Å)	8.689(3)	8.8285(5)	1.6
c (Å)	9.067(9)	8.9360(5)	−1.4
α (deg)	89.44(6)	90.0	0.6
β (deg)	123.78(7)	124.779	0.8
γ (deg)	90.61(6)	90.0	−0.7
V (Å^3)	999.5	990.9	−0.9

[a] For comparison, parameters of the rhombohedral phase are referred to a monoclinic C-centered cell. Variation of the parameters with the phase transition is also included.

The change in symmetry is accompanied by a variation of the lattice dimensions. The parameters of the rhombohedral phase are compared with those of the triclinic phase in Table 1. Some of them increase while others decrease; however, the resulting cell volume increases slightly for the low-temperature phase in contrast to that observed for $LiSn_2(PO_4)_3$.[14] A comparison of the structural modifications with those of the low-symmetry phase of $LiZr_2(PO_4)_3$ is not possible because, although a similar phase transition has been reported by different authors, at present, the low-symmetry phase has not been indexed.[4,5,17,18]

The rhombohedral phase can be obtained again by raising the sample temperature. This fact indicates that the phase transition is reversible. The variation observed for the cell volume together with the discontinuity found in the DSC curves support a first-order character for the phase transition. Moreover, a small hysteresis has been detected from the DSC curves in the heating and cooling runs. This is similar to that reported for $LiZr_2(PO_4)_3$[17] but differs from the large hysteresis cycle found for $LiSn_2(PO_4)_3$.[14] The enthalpy associated with the phase transition of $LiHf_2(PO_4)_3$ (4.5 kJ/mol) is lower than those of $LiZr_2(PO_4)_3$ (∼6.6 kJ/mol) and $LiSn_2(PO_4)_3$ (∼7.9 kJ/mol).

IV.2. Lithium Location. Determination of the lithium positions in the structure is difficult to obtain from XRD data due to its low scattering factor. In this case, ^{7}Li NMR can be used to analyze structural sites occupied by lithium.

As deduced from NMR and conductivity data, lithium mobility in the triclinic phase is very low (see section IV.3). Then, the existence of a single central line with a unique quadrupole pattern in the ^{7}Li NMR spectra of the sample cooled at −23 °C supports that lithium ions occupy only one type of site in this phase. From C_Q and η constants, distortions of the lithium environment can be estimated. In particular, the observed C_Q and η values in the triclinic $LiHf_2(PO_4)_3$ phase ($C_Q = 180$ kHz, $\eta = 0.3$) are much higher than those reported at low temperatures for lithium in the rhombohedral $LiTi_2(PO_4)_3$[28] ($C_Q = 15$ kHz, $\eta = 0$). As structural distortions

(26) Křivý, I.; Gruber, B. *Acta Crystallogr.* **1976**, *A32*, 297.
(27) Losilla, E. R.; Aranda, M. A. G.; Martínez-Lara, M.; Bruque, S., manuscript in preparation.

Table 2. Experimental and Estimated Second Moment Values Corresponding to Lithium Occupying the M_1 and M_2 Sites[a]

M_2 site					M_1 site					experimental
$\Delta\bar{\omega}^2_{total}$ [G²]	$\Delta\bar{\omega}^2_{Li-P}$ [G²]	$\Delta\bar{\omega}^2_{Li-Li}$ [G²]	r_{Li-P} [Å]	r_{Li-Li} [Å]	$\Delta\bar{\omega}^2_{total}$ [G²]	$\Delta\bar{\omega}^2_{Li-P}$ [G²]	$\Delta\bar{\omega}^2_{Li-Li}$ [G²]	r_{Li-P} [Å]	r_{Li-Li} [Å]	$\Delta\bar{\omega}^2$ [G²]
0.30	0.27	0.03	2.66 3.49	6.27	0.10	0.07	0.03	3.64	6.27	0.36 ± 0.03

[a] The experimental value was deduced from the central transition of ^{7}Li NMR static spectra of the triclinic phase. Relative Li−Li and Li−P contributions ($\Delta\bar{\omega}^2_{Li-Li}$, $\Delta\bar{\omega}^2_{Li-P}$) to the total estimated second moment were calculated with expression (2) of the text.

are always higher in M_2 sites than in M_1 sites, ^{7}Li NMR data suggest that, in the absence of ionic motion, lithium ions could occupy sites with lower symmetry (probaly M_2 sites) in the triclinic $LiHf_2(PO_4)_3$ than in rhombohedral $LiTi_2(PO_4)_3$, at which occupation of M_1 sites was deduced by neutron diffraction and NMR techniques.[28−30]

This is also supported by the analysis of the experimental second moment ($\Delta\bar{\omega}^2$), $\Delta\bar{\omega}^2 = 2/(T_2)^2$, of the central transition of the ^{7}Li static NMR spectrum recorded at −23 °C, at which lithium mobility is very low (see section IV.3). As broadening of this line is generally caused by dipolar interaction between neighbor nuclei, the experimental second moment of this phase can be compared with those calculated for different lithium locations by using the Van Vleck expression for a rigid lattice in powder samples:[31]

$$\Delta\bar{\omega}^2 = \frac{3}{5}\gamma_I^4\hbar^2 I(I+1)\sum_k \frac{1}{r_{jk}^6} + \frac{4}{15}\gamma_I^2\gamma_S^2\hbar^2 S(S+1)\sum_k \frac{1}{r_{jk}^6} \quad (2)$$

The first term accounts for dipolar interactions between like spins and the second one between unlike spins. γ_I and γ_S are the gyromagnetic ratios for the I and S spins and r_{jk} is the distance between interacting spins. Taking into account the low gyromagnetic ratios of the other nuclei present in this compound, the Li−Li and Li−P dipolar interactions are the most important contributions to the second moment of the central line of ^{7}Li NMR spectra of $LiHf_2(PO_4)_3$. The Li−Li and Li−P distances for the triclinic phase were calculated by using the relative atomic coordinates determined for the rhombohedral $LiZr_2(PO_4)_3$[17] and the lattice dimensions of the rhombohedral $LiHf_2(PO_4)_3$ phase. This procedure was adopted because (i) there are no atomic coordinates available for the low-symmetry phases of $LiM^{IV}_2(PO_4)_3$ family, (ii) lattice parameters of the low- and high-temperature phases of $LiHf_2(PO_4)_3$ are very close and, therefore, interatomic distances should not change significantly between both phases, and (iii) Zr^{4+} and Hf^{4+} show similar ionic radii.

The second moment estimated for lithium ions occupying the M_1 and M_2 sites are shown and compared with the experimental $\Delta\bar{\omega}^2$ in Table 2. A good agreement between the experimental and calculated second moment for lithium in the M_2 sites is obtained. This suggests that lithium could be preferentially placed in M_2 sites, in agreement with the conclusions deduced from the previous analysis of C_Q and η values.

IV.3. Lithium Mobility. From NMR and conductivity data, an important variation on lithium mobility has been detected at the phase transition. In the triclinic phase, T_2^{-1} and T_1^{-1} are characteristic of lithium ions with low mobility. In particular, T_2^{-1}, which is mainly governed by dipolar interaction among magnetic moments of nuclei, does not change with temperature, indicating that residence time of lithium at sructural sites is long enough to avoid that interaction of lithium with other nuclei be averaged by motion. Moreover, the nearly temperature-independent behavior of T_1^{-1}, with long T_1 values, is generally ascribed to nuclear relaxation through paramagnetic impurities when lithium-ion mobility is not significant enough to dominate relaxation behavior.[32] In addition, the ionic conductivity is rather low ($<10^{-7}$ Ω^{-1} cm^{-1}) and the activation energy very high (1.39 eV), supporting again that lithium mobility in this phase is very low.

Above 0 °C, i.e., at temperatures at which the sample is transformed into the rhombohedral polymorph, a very significant increase of lithium mobility is detected:

(i) T_2^{-1}, proportional to the line width of the central line, decreases considerably and the line shape changes from Gaussian to Lorentzian. These facts indicate a strong reduction of the time spent by lithium at the initial sites, which leads to the partial cancellation of the Li−P dipolar interactions (motional line narrowing).

(ii) The spin−lattice relaxation rate, T_1^{-1}, increases enormously. Diffusive motion of lithium ions is a powerful source of fluctuating fields and, therefore, the most probable cause of the strong increase of the relaxation rate in the rhombohedral phase. The broad maximum observed in the T_1^{-1} curve suggests a complex relaxation mechanism for the rhombohedral phase that is difficult to analyze.

(iii) The bulk conductivity increases about 2 orders of magnitude and the activation energy decreases to 0.33 eV for the rhombohedral phase. This value is much lower than that obtained in the triclinic phase (1.39 eV), showing that the movement of lithium ions becomes easier in the NASICON framework of the rhombohedral phase. This fact suggests that the structural changes involved at the phase transition induce a modification of the conduction channels, probably at the bottleneck betwen M_1 and M_2 sites, that favors the movement of lithium ions. On the other hand, the abrupt change of ionic conductivity around 0 °C supports the first-order character of the phase transition,[33] which is in agreement with the conclusions deduced previously from DSC and XRD techniques.

(28) París, M. A.; Martínez-Juárez, A.; Rojo, J. M.; Sanz, J. *J. Phys.: Condens. Matter* **1996**, *8*, 5355.
(29) París, M. A.; Sanz, J. *Phys. Rev. B*, in press.
(30) Tran Qui, D.; Hamdoune, S.; Souberyroux, J. L.; Prince, E. J. *Solid State Chem.* **1988**, *72*, 309.
(31) Van Vleck, J. H. *Phys. Rev.* **1948**, *74*, 1168.
(32) Verber, C. M.; Mahon, H. P.; Tanttila, W. H. *Phys. Rev.* **1962**, *125*, 1149.
(33) Goodenough, J. B., Ruiz-Diaz, J. E., Zhen, Y. S. *Solid State Ionics* **1990**, *44*, 21.
(34) Sanz, J.; Rojo, J. M.; Iglesias, J. E.; Alamo, J. *Solid State Ionics* **1993**, *62*, 287.

On the other hand, the observation of an unique line in the ^{7}Li MAS NMR spectra of the rhombohedral $LiHf_2(PO_4)_3$ phase suggests the existence of a fast motion of lithium that averages the line positions corresponding to M_2 and M_1 sites (exchange process). In fact, two lines associated with lithium in these two crystallographic sites have been previously detected in $LiSn_2(PO_4)_3$[14] and $LiZr_2(PO_4)_3$.[34] The line with higher chemical shift value was assigned to lithium at the M_2 site and the other to lithium at the M_1 site. The progressive delocalization of lithium, probably placed at M_2 sites in the triclinic phase, between both structural sites would be responsible for the slight but systematic shift toward lower values observed for the central ^{7}Li MAS NMR line during the phase transition.

The delocalization of lithium over two sites can also be analyzed through the evolution of C_Q with temperature. In the case of a fast exchange between M_1 and M_2 sites, the observed C_Q constant would be governed by the expression

$$C_Q = \frac{C_Q^{(1)}P_1 + C_Q{}^{(2)}3P_2}{P_1 + 3P_2} \qquad (3)$$

where P_1 and P_2 are the occupation probability of M_1 and M_2 sites, $C_Q^{(1)}$ and $C_Q^{(2)}$ the quadrupole coupling constant associated with each site, and the factor 3 takes into account the different multiplicity of both sites. In the rhombohedral $LiHf_2(PO_4)_3$ phase, C_Q does not change significantly with temperature, indicating that P_1 and P_2 do not change above the phase transition temperature. Moreover, if the $C_Q^{(2)}$ value is assumed to be that of the triclinic phase (180 kHz) and $C_Q^{(1)}$ to be close to the measured value at low-temperature in $LiTi_2(PO_4)_3$[27] (15 kHz), the value calculated (138 kHz) on the basis of maximum delocalization of lithium ions ($P_1 = P_2 = 0.25$) agrees quite well with the experimental one ($\approx$120 kHz). The previous calculation is based on the hypothesis that all rhombohedral phases exhibit similar quadrupole interactions at each structural site (M_1 and M_2) and do not differ considerably from that of the triclinic $LiHf_2(PO_4)_3$ phase. Finally, the proposed fast exchange model between the two sites would give an η value near zero, which is also experimentally confirmed. All these experimental observations support the assumptions about high delocalization of lithium on M_1 and M_2 sites and explain the high conductiviy values measured in the rhombohedral phase of $LiHf_2(PO_4)_3$.

V. Conclusions

A reversible first-order phase transition has been detected in the $LiHf_2(PO_4)_3$ compound when cooled through 0 °C, yielding a change of the crystal symmetry from rhombohedral to triclinic. In this transformation, the associated enthalpy is 4.5 kJ/mol.

From XRD data, the obtained lattice parameters for the low-temperature phase are $a = 15.26(1)$, $b = 8.689(3)$, $c = 9.067(9)$ Å, $\alpha = 89.44(6)°$, $\beta = 123.78(7)°$, $\gamma = 90.61(6)°$. The triclinic distortion of the NASICON framework produces a splitting of the initial ^{31}P MAS NMR single line of the rhombohedral phase into three components, indicating an increase in the number of independent crystallographic P sites. In this phase, lithium ions are located at sites with lower symmetry (probably M_2 sites) than in rhombohedral $LiTi_2(PO_4)_3$ (M_1 sites) as deduced from the analysis of the central line and the quadrupole pattern of ^{7}Li NMR spectra. Finally, ionic mobility is very low as inferred from conductivity and T_1 and T_2 NMR relaxation data.

Above the phase transition temperature, the rhombohedral $R\bar{3}c$ lattice is recovered and an abrupt increase of the ionic mobility is detected. Thus, T_2^{-1} and T_1^{-1} relaxation rates and dc ionic conductivity change drastically around 0 °C. Moreover, the activation energy obtained from bulk conductivity data decreases from 1.39 eV for the triclinic phase to 0.33 for the rhombohedral one. Finally, from evolution of the quadrupole coupling constant of ^{7}Li NMR spectra with temperature, a strong delocalization of lithium over M_1 and M_2 sites has been deduced for the rhombohedral phase.

Acknowledgment. Financial support by CICYT of Spain (Project MAT95-0899) is gratefully acknowledged.

CM9700413